Journal of Materials Chemistry A

ROYAL SOCIETY OF CHEMISTRY

PAPER

View Article Online
View Journal

Cite this: DOI: 10.1039/d5ta10430k

Dopant-controlled transition-metal ordering in high-voltage spinel cathodes

Li Zhang, [abc] Beth E. Murdock, [abc] Xiao Hua [ac] and Nuria Tapia-Ruiz *[bc]

Received 23rd December 2025
Accepted 19th January 2026

DOI: 10.1039/d5ta10430k

rsc.li/materials-a

The ongoing advancement of rechargeable batteries has motivated extensive efforts to optimise cathode materials through targeted chemical doping to enhance electrochemical performance. Yet, the atomic-scale consequences of transition metal substitution, particularly its influence on atomic arrangement and/or cation ordering, remain insufficiently understood. A central challenge arises because transition metal dopants frequently occupy the same crystallographic site as the host transition metal species, complicating the analysis of the resulting cation distribution. Previous neutron pair distribution function (NPDF) investigations of the spinel cathode $LiMn_{1.5}Ni_{0.5}O_4$ have shown that comparing local (short-range) and average (long-range) site occupancies of Mn and Ni can provide valuable insight into transition metal arrangements. Building upon this strategy, the present work employs NPDF to examine how Fe doping modifies lattice parameters and cation ordering within the spinel framework. Fe substitution is particularly attractive because it offers cost advantages and has been linked to improved electrochemical performance. This study identifies how Fe incorporation modifies the site occupancy of Mn and Ni, determines the preferential lattice sites adopted by Fe, and establishes an analytical framework for disentangling dopant-induced structural modifications in oxide cathodes.

1. Introduction

The rapid expansion of the electric vehicle industry, driven by the imperative to reduce greenhouse gas emissions, has intensified research into high-performance and sustainable lithium-ion batteries. Among the components of these systems, cathode materials play a central role in this technology as they not only determine the achievable energy density and cycling performance but also exert a strong influence on the overall manufacturing cost.[1]

One widely adopted approach to enhance cathode performance is cation substitution, which enables fine-tuning of composition and structure to improve electrochemical behaviour through modulation of redox processes, structural evolution and ion diffusion pathways.[2–4] Among commonly explored dopants, iron is particularly attractive due to its natural abundance, low cost, and environmentally benign character. Its favourable metal–oxygen bond covalency facilitates redox activation and has been shown to enhance cycling stability and rate capability.[5,6] Although numerous studies have shown that dopants can improve morphology and structural stability, among others, the influence of substituted cations on the local atomic arrangements, particularly transition metal (TM) ordering, remains poorly understood.[7–9]

Alkali-metal (AM) transition metal oxides with inherently good electronic conductivity represent one of the most promising families of cathode materials for commercial deployment.[10–12] Their crystal structures are fundamentally governed by the alkali-to-metal ratio, where for lithium-based cathodes with formula $Li_{1+x}TM_{1-x}O_2$ ($0 \leq x \leq 1/3$), compositions adopt layered or disordered rocksalt structures, whereas $LiTM_2O_4$ materials crystallise in the spinel structure.[13,14] For sodium oxide-based cathodes, *e.g.*, Na_xTMO_2 ($0.44 \leq x \leq 1$), compositions generally exhibit layered structures, though the stacking arrangement and Na coordination environments differ substantially from those in Li analogues.[15]

Building on these structural insights, detailed structural analyses have shown, for example, that species such as Ni and Mg can partially occupy AM sites in some layered oxide compositions, displacing alkali ions into TM layers and thereby altering the local atomic environment.[16,17] These findings highlight that cation distributions can be highly complex and, as a result, are often difficult to distinguish by conventional X-ray or neutron diffraction. This is a significant issue because cation ordering is widely recognised as a key determinant of electrochemical performance.[18–23] This becomes even more pronounced in multicomponent oxides, where dopant distributions may be heterogeneous and subtle variations in local structure can exert significant electrochemical consequences.[24] Advanced techniques such as reverse Monte Carlo (RMC)

[a]Department of Chemistry, Lancaster University, Lancaster LA1 4YB, UK
[b]Department of Chemistry, Molecular Sciences Research Hub, White City Campus, Imperial College London, London W12 0BZ, UK. E-mail: n.tapia-ruiz@imperial.ac.uk
[c]The Faraday Institution, Quad One, Harwell Science and Innovation Campus, Didcot OX11 0RA, UK

modelling combined with pair distribution function (PDF) analysis have emerged as powerful tools for probing short-range order, yet further methodological refinement is required to reliably capture TM configurations in these complex systems.[25,26] Addressing this gap, by clarifying how dopants influence cation ordering, would enable stronger structure–property correlations and guide the rational design of next-generation cathode compositions.

TM ordering in the high-voltage $LiMn_{1.5}Ni_{0.5}O_4$ (LMNO) spinel plays a decisive role in defining Li-ion transport pathways, redox accessibility, and long-range structural stability.[27] While LMNO is often described as ordered or disordered, recent neutron PDF studies have demonstrated that ordering is highly length-scale dependent: local Mn/Ni arrangements remain largely intact at short distances, whereas substantial cation disorder emerges beyond ≈10–20 Å.[28] This structural heterogeneity originates from inter-unit Mn–Ni exchange processes and produces domains with differing TM compositions that are invisible to average crystallographic models. Consequently, probing LMNO across multiple real-space windows is essential for identifying the true distribution of Mn, Ni, and dopant/substituent atoms, as well as understanding their influence on electrochemical behaviour.

In parallel, cation substitution has emerged as an effective strategy for tuning the structural and electrochemical characteristics of spinel cathodes.[32,33] By adjusting the local bonding environment, modulating oxygen coordination, and altering the valence states of TM atoms, substituents can stabilise the spinel framework, regulate redox chemistry, and enhance Li-ion transport. Fe, in particular, offers unique advantages due to its natural abundance, stability in the Fe^{3+} state, favourable metal–oxygen bond covalency, and demonstrated ability to influence Mn and Ni valence states.[29–31] Prior studies have shown that introducing Fe into LMNO can improve cycling stability, modify redox potentials, and expand the Mn^{3+}/Mn^{4+} contribution near 4.1–4.2 V, thereby tuning both lattice parameters and electrochemical behaviour.[32]

To accurately resolve these structural subtleties, real-space PDF analysis using the $P4_332$ structural model is essential.[28] Unlike the commonly adopted $Fd\bar{3}m$ model, which places Mn and Ni on the same 16*d* site and therefore masks important cation redistributions, the $P4_332$ symmetry explicitly distinguishes Mn and Ni within the 12*d* and 4*b* sites, respectively. This site specificity enables detailed interrogation of TM ordering across short-, intermediate-, and long-range environments, providing a powerful platform for understanding how thermal treatment, compositional tuning, and targeted Fe substitution reshape the structural landscape of LMNO. Moreover, structural connections among layered, spinel, and rock-salt Li-oxide cathodes provide a broader context for understanding these effects.[33–36] Such structural relationships highlight the importance of understanding how dopants, particularly in this case, redox-active species like Fe, shape the evolution of local TM environments.[32,33]

In this work, we combine multiscale neutron PDF (NPDF) analysis with systematic Fe substitution to investigate how dopants redistribute within the spinel lattice and how these rearrangements correlate with electrochemical behaviour. By examining both Ni-substituted $LiMn_{1.5}Ni_{0.5-2x}Fe_{2x}O_4$ and Mn/Ni co-substituted $LiMn_{1.5-x}Ni_{0.5-x}Fe_{2x}O_4$ (x = 0.05 and 0.1) compositions, and comparing post-annealed (PA) and non-annealed (NA) LMNO, we directly track the evolution of Mn, Ni, and Fe occupancies from the local (1–6.5 Å) to extended (5–40 Å) structural regimes. This approach reveals how Fe dopants alter Mn/Ni ordering, how cation–exchange processes propagate across structural domains, and how these modifications influence the electrochemical behaviour of these materials. Through this combined structural–electrochemical framework, we provide new insights into the design of high-performance spinel cathodes based on controlled TM ordering and site-selective doping.

2. Experimental

2.1. Synthesis

$LiMn_{1.5}Ni_{0.5}O_4$ and Fe-substituted $LiMn_{1.5-x}Ni_{0.5-x}Fe_{2x}O_4$ and $LiMn_{1.5}Ni_{0.5-2x}Fe_{2x}O_4$ (x = 0.05 and 0.1) samples were prepared *via* a solution-assisted route using stoichiometric amounts of lithium acetate (Alfa Aesar, 99%), nickel acetate (Aldrich, 99%), manganese acetate (Aldrich, 99%) iron nitrate (Alfa Aesar, 98%) and oxalic acid (Alfa Aesar, 98%) as reagents. Precursor solutions were prepared with a 1 : 1 molar ratio of oxalic acid to total cations, stirred for 2 h at ambient temperature, and dried overnight in a 50 °C water bath under continuous stirring. The resulting precipitates were preheated at 500 °C for 6 h to remove residual organics.

For $LiMn_{1.5}Ni_{0.5}O_4$ and Fe-substituted materials, the preheated powders were pelletised under a pressure of 5 N cm^{-2} and calcined at 900 °C for 24 h without post-annealing, using heating and cooling rates of 10 °C min^{-1}. The obtained $LiMn_{1.5}Ni_{0.5}O_4$ is referred to as non-annealed LMNO (NA-LMNO). A second batch of $LiMn_{1.5}Ni_{0.5}O_4$ was calcined at 900 °C for 24 h, followed by post-annealing at 700 °C for 48 h, with heating and cooling rates of 3 °C min^{-1} and 1 °C min^{-1}, respectively. This sample is designated as post-annealed LMNO (PA-LMNO).[29]

2.2. Time-of-flight neutron pair distribution function analysis

Time-of-flight neutron PDF measurements were performed on all six spinel samples using the General Materials (GEM) diffractometer at the ISIS Neutron and Muon Source.[37] Powdered samples were loaded into cylindrical vanadium canisters ($ø$ = 6 mm, h = 5.5 cm) in an Ar-filled MBraun glovebox (H_2O and O_2 < 0.1 ppm). Data were collected over a Q-range of 0.01–50 Å across multiple detector banks. An 8 h collection time per sample ensured a high signal-to-noise ratio at a high Q. To enable accurate background subtraction, intensity scaling and instrument correction, a series of dedicated calibration measurements were also collected. These included: (i) an empty 6 mm vanadium can (≈4 h total), to characterise scattering from the sample container; (ii) an 8 mm vanadium–niobium calibration rod (≈4 h total), used to

determine detector efficiency and the wavelength-dependent instrument response; and (iii) an empty-instrument run with no sample or can in the beam (≈2 h), to capture baseline instrument and environmental scattering. All raw data were processed and normalised using the Gudrun software package, which implements detector correction, multiple scattering, container subtraction and Fourier transformation into real space.[38] Subsequent PDF refinements were carried out using the PDFgui software.[39]

2.3. Electrochemistry

Spinel materials were mixed with carbon black (Super P, IMCAL) and polyvinylidene difluoride (PVDF, MTI) in a weight ratio of 80 : 10 : 10 using a planetary ball mill (TOB energy). PVDF was dissolved in *N*-methyl-2-pyrrolidone (NMP, 99.9%, Aladdin) to make a 5 wt% solution. Slurries were cast onto Al foil (16 μm, 99.45%, TOB New Energy) using a doctor blade and dried overnight at 80 °C. Electrodes of 12 mm diameter were punched, pressed at 3 N using a hydraulic press, and vacuum dried at 120 °C overnight before they were transferred into an Ar-filled MBraun glovebox (<0.1 ppm H_2O and O_2). The mass loading of the active materials was approximately 2.8 mg cm^{-2}.

CR2032 coin cells were assembled using lithium metal chips (99.99%, TOB New Energy) as counter electrodes, 1 M $LiPF_6$ in EC/DMC (1 : 1 v/v, Sigma-Aldrich) as electrolyte, and glass fiber separators (Whatman, GF/F). Galvanostatic cycling was performed at room temperature using a Neware CT-4008Tn system at 1C (1C = 147 mA g^{-1}) over a voltage window of 3.5–4.9 V.

3. Results and discussion

3.1. Local order and extended disorder in LMNO materials

Previous studies using quantitative modelling of the PDF as a function of real-space length scale (*via* so-called r-dependent or "box-car" style fitting) have established that post-annealed LMNO displays a well-defined ordered transition metal arrangement, whereas the non-post-annealed counterpart exhibits a pronounced Mn/Ni disorder above 6 Å approximately.[28] Building on this understanding, this work examines atomic ordering over local and extended ranges (1–6.5 Å, 5–20 Å, and 5–40 Å), using NPDF analysis to characterise cation distribution.

All NPDF refinements of LMNO were carried out using the $P4_332$ structural model (Fig. 1, S1 and S2), which assigns Mn and Ni to crystallographically distinct 12*d* and 4*b* sites, respectively (Fig. 1b, left). In contrast, $Fd\bar{3}m$ locates both cations on the same 16*d* site (Fig. 1b, right). As the Mn/Ni disorder increases, Mn occupancy on the 12*d* sites decreases while its occupancy on the 4*b* site increases; complete disorder corresponds to 75% Mn occupancy on both sites. When Mn occupation on the 12*d* sites falls below this threshold, some unit cells necessarily accommodate fully Mn-occupied 4*b* sites, leading to a combination of intra-unit cell and inter-unit cell disorder motifs.

The NPDF patterns of PA- and NA-LMNO (Fig. 1a and c) reveal that both materials exhibit highly similar local structures over the 1–6.5 Å range, whereas substantial divergences appear at intermediate and extended ranges (5–40 Å). This is consistent with reported NPDF results of ordered and disordered LMNO.[28] Following established refinement protocols for spinel LMNO, the Mn/Ni occupancies were constrained during fitting (Table S1), where the Ni-4*b* occupancy ($occTM_1$) defines all other site fractions: Mn-4$b = (1 - occTM_1)$, Ni-12$d = (1 - occTM_1)/3$, and Mn-12$d = (2 + occTM_1)/3$.

Short-range NPDF refinements (1–6.5 Å) indicate that both PA-LMNO and NA-LMNO retain predominantly ordered cation arrangements, with only a minor degree of local TM mixing. Mn occupies the 12*d* sites at 99.58% in PA-LMNO and 97.13% in NA-LMNO (Tables S4 and S5), confirming that the Mn–O and Ni–O

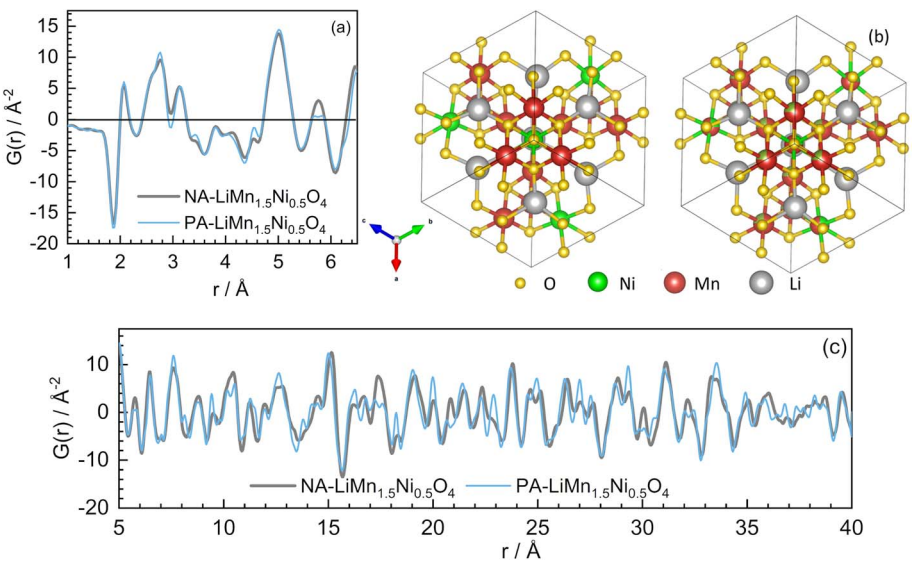

Fig. 1 Neutron pair distribution function profiles for post-annealed (PA) $LiMn_{1.5}Ni_{0.5}O_4$ and non-annealed (NA) $LiMn_{1.5}Ni_{0.5}O_4$ over 1–6.5 Å (a) and 5–40 Å (c), with corresponding schematic representations of the local structure of LMNO polymorphs: $P4_332$ (left) and $Fd\bar{3}m$ (right) (b).

coordination environments remain largely intact immediately surrounding each TM atom.

However, a clear structural divergence emerges as the fitting range is extended. Over 5–40 Å, PA-LMNO maintains a highly ordered TM configuration, with Mn occupancy on the 12*d* sites remaining at 95.70%. In contrast, NA-LMNO shows a pronounced increase in disorder, with Mn-12*d* occupancy falling to 77.38%, approaching the statistical limit for complete Mn/Ni disorder. This pronounced redistribution across the 12*d* and 4*b* sites in NA-LMNO highlights the coexistence of locally ordered domains embedded within a disordered matrix and provides a sensitive platform for probing dopant-driven cation rearrangement and preferential site occupancy in subsequent Fe-substituted compositions.

3.2. Impact of Fe substitution on local structure

Fig. 2 compares the NPDF data of Fe-substituted LMNO samples: $LiMn_{1.5}Ni_{0.5-2x}Fe_{2x}O_4$ (Fe replacing Ni) and $LiMn_{1.5-x}Ni_{0.5-x}Fe_{2x}O_4$ (Fe replacing Mn and Ni), where x = 0.05 and 0.1, with NA-LMNO. In the 1–6.5 Å region, all Fe-substituted materials closely resemble NA-LMNO, apart from subtle intensity variations near 5 Å (Fig. 2a and b). Similarly, in the 5–40 Å region, their NPDF data closely match NA-LMNO rather than PA-LMNO (Fig. 1c, 2c and d). Nonetheless, differences in peak intensities and positions reveal clear variations in lattice parameters and cation distribution upon Fe incorporation. These are discussed quantitatively based on the PDF fitting results shown in Fig. S3–S6 and Tables S4–S9.

To evaluate Fe site preference, two structural models were tested: Model 1, with Fe initially placed on the 4*b* site; and Model 2, with Fe initially located at the 12*d* site (Table 1). The initial structural models were constructed with Mn and Ni fully occupying the 12*d* and 4*b* sites, respectively. For simplicity, the total octahedral site occupancies were constrained to equal 1, although true occupancies may be reduced by cation loss to impurity phases or by anti-site defects that place TMs on tetrahedral Li 8*a* sites. This simplification is justified because the impurity concentration in the Fe-substituted samples is negligible, as evidenced by the X-ray diffraction patterns shown in Fig. S7. Moreover, although anti-site defects are present (≈2% TM on the Li site), as reported previously, their concentration does not vary with Fe content.[29] Subsequently, site exchange of TM atoms between the 12*d* and 4*b* sites was allowed using the initial Fe/Mn or Fe/Ni ratios listed in Table 1, thereby allowing all three TM atoms to occupy both sites. The occupancy rates of TM atoms in Fe-substituted materials are summarised in Tables S2 and S3.

Ni occupancy became unphysical (negative) in Model 2 during refinements of Mn/Ni co-substituted compositions,

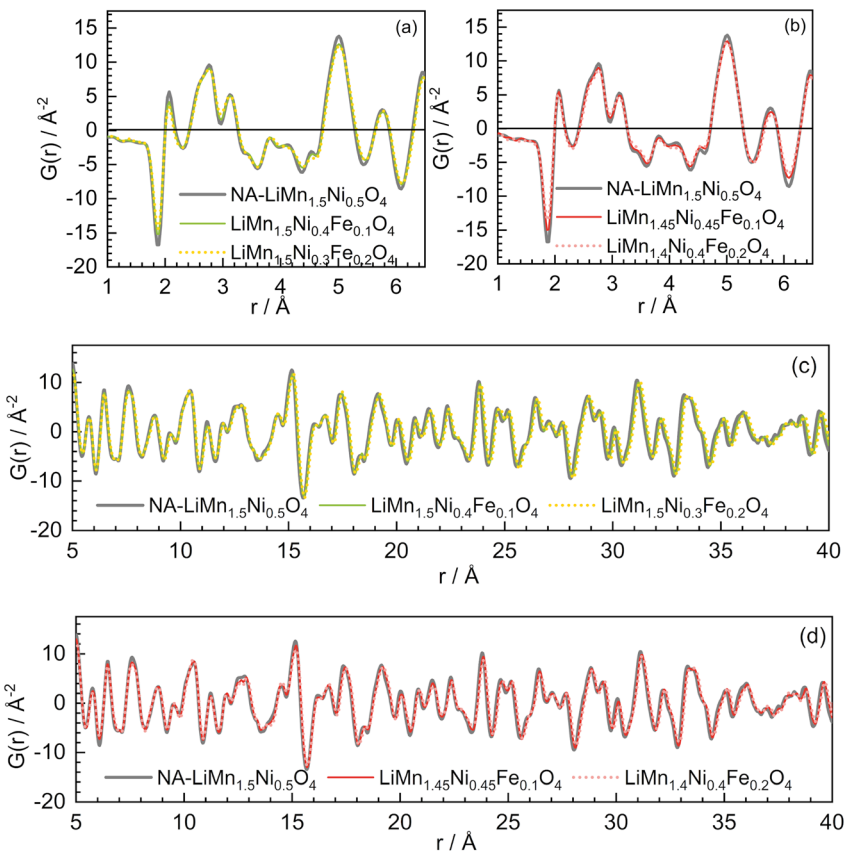

Fig. 2 Neutron pair distribution function profiles of Fe-substituted spinel compositions: $LiMn_{1.5}Ni_{0.4}Fe_{0.1}O_4$ and $LiMn_{1.5}Ni_{0.3}Fe_{0.2}O_4$ in the ranges 1–6.5 Å (a) and 5–40 Å (c), and $LiMn_{1.45}Ni_{0.45}Fe_{0.1}O_4$ and $LiMn_{1.4}Ni_{0.4}Fe_{0.2}O_4$ in the ranges 1–6.5 Å (b) and 5–40 Å (d). All profiles are compared to non-annealed (NA) $LiMn_{1.5}Ni_{0.5}O_4$.

Table 1 Initial transition metal atom configurations on the 12*d* and 4*b* sites used for NPDF fitting of Fe-substituted spinel materials

	Model 1 – Fe in 4*b*-site						Model 2 – Fe in 12*d*-site					
	12*d* site			4*b* site			12*d* site			4*b* site		
Occupancy rates (×100%)	Mn	Ni	Fe	Mn	Ni	Fe	Mn	Ni	Fe	Mn	Ni	Fe
$LiMn_{1.5}Ni_{0.4}Fe_{0.1}O_4$	1	0	0	0	4/5	1/5	14/15	0	1/15	1/5	4/5	0
$LiMn_{1.5}Ni_{0.3}Fe_{0.2}O_4$	1	0	0	0	3/5	2/5	13/15	0	2/15	2/5	3/5	0
$LiMn_{1.45}Ni_{0.45}Fe_{0.1}O_4$	29/30	1/30	0	0	4/5	1/5	14/15	0	1/15	1/10	9/10	0
$LiMn_{1.4}Ni_{0.4}Fe_{0.2}O_4$	14/15	1/15	0	0	3/5	2/5	13/15	0	2/15	1/5	4/5	0

indicating that Fe substitution favours the Ni site (4*b*) rather than the Mn site (12*d*). Thus, Model 1 was adopted for all Fe-substituted materials. We note that the individual site occupancies of Ni and Fe cannot be determined with high confidence due to their similar coherent neutron scattering lengths.[40] Consequently, their refined occupancies should be interpreted as reflecting relative trends rather than absolute values. Nevertheless, the collective refinement consistently indicates a strong preferential substitution of Fe on the Ni sites, with only minor variation in this preference as the overall Fe content increases. This also suggests that despite the intrinsic limitation of neutron scattering, a comparative analysis across a systematic composition series still yields convincing composition-dependent structural information to enable identification of important site-substitution behaviour in our materials.

3.3. Lattice evolution upon Fe substitution

Lattice parameters extracted from NPDF refinements over three real-space ranges (1–6.5 Å, 5–20 Å and 5–40 Å) for all the samples in this study are shown in Fig. 3a. All samples retain the expected cubic symmetry. In the short-range regime (1–6.5 Å), PA-LMNO exhibits a marginally larger lattice parameter (8.149 Å) than NA-LMNO (8.144 Å) which might reflect local variations in Mn/Ni configurations. Based on the reported modelling strategy, the $P4_332$ space group can generate four distinct Mn/Ni ordering types (A1–A4) (Fig. 3b). An ideal ordering corresponds to a single specific configuration (A1), whereas a disordered spinel comprises a statistical mixture of all four arrangements.[28] NPDF refinements confirm that PA-LMNO, while more ordered overall, still contains a minor fraction of alternative configurations, consistent with the incomplete Mn occupancy of the 12*d* sites observed across both short- (1–6.5 Å) and long-range (5–40 Å) fitting windows.

As the fitting range increases from 5–20 to 5–40 Å, PA-LMNO and NA-LMNO display divergent lattice evolution trends (Fig. 3a). The opposing behaviours reflect differences in how the four configuration units accumulate and propagate across longer structural length scales. NA-LMNO, in particular, shows a greater degree of structural complexity, indicative of more pervasive and correlated disorder within the A1–A4 network.

These observations are consistent with prior studies reporting that post-annealing reduces the oxygen-vacancy concentration in LMNO.[41,42] Charge neutrality is maintained predominantly through $Mn^{4+} \rightarrow Mn^{3+}$ reduction, which decreases Mn–O electrostatic attraction and shortens Mn–cation distances. Such changes in local bonding geometry manifest directly in the interatomic distances obtained from PDF analysis and correlate with the refined site occupancies reported in Tables S4 and S5.

All four Fe-substituted samples exhibit systematically larger lattice parameters than LMNO across all fitting ranges (Fig. 3a and Tables S6–S9). For instance, in the short-range window, the lattice parameter (*a*) increases to 8.162 Å ($LiMn_{1.5}Ni_{0.4}Fe_{0.1}O_4$), 8.177 Å ($LiMn_{1.5}Ni_{0.3}Fe_{0.2}O_4$), 8.160 Å ($LiMn_{1.45}Ni_{0.45}Fe_{0.1}O_4$), and 8.169 Å ($LiMn_{1.4}Ni_{0.4}Fe_{0.2}O_4$). These lattice differences

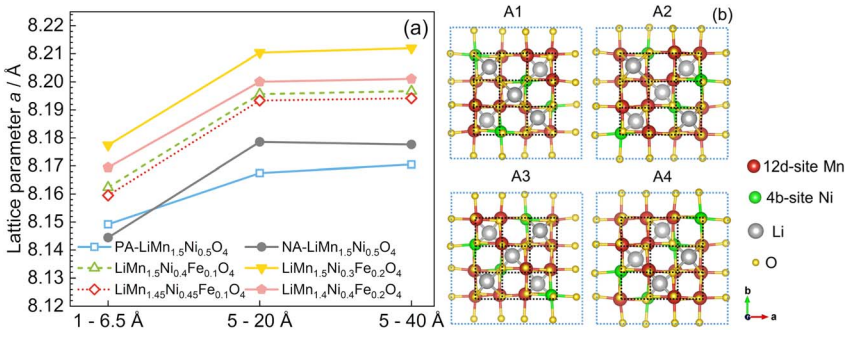

Fig. 3 Lattice parameters of PA-$LiMn_{1.5}Ni_{0.5}O_4$, NA-$LiMn_{1.5}Ni_{0.5}O_4$, and Fe-substituted $LiMn_{1.5}Ni_{0.4}Fe_{0.1}O_4$, $LiMn_{1.5}Ni_{0.3}Fe_{0.2}O_4$, $LiMn_{1.45}Ni_{0.45}Fe_{0.1}O_4$ and $LiMn_{1.4}Ni_{0.4}Fe_{0.2}O_4$ compositions obtained by fitting their neutron pair distribution function data over 1–6.5 Å, 5–20 Å, and 5–40 Å, using the $P4_332$ structural model (a), and schematic representations of spinel structures indexed to the $P4_332$ space group in the range up to 6.5 Å viewed along the *c* axis (b).

indicate two clear trends: (a) for a fixed Fe concentration, Ni-substituted compositions exhibit larger lattice parameters than Mn/Ni co-substituted materials; and (b) for both substitution routes, increasing Fe content leads to progressively larger lattice parameters. The consistency of these trends across all fitting ranges (1–6.5 Å, 5–20 Å, and 5–40 Å), and their agreement with published neutron diffraction data on Fe-substituted LMNO, underscores their robustness.[29]

The lattice expansion in these samples is governed by the valence states and charge-compensation mechanisms associated with Fe incorporation. Previous work shows that Fe adopts the Fe^{3+} valence state in LMNO when substituted.[30,31] In Ni-substituted materials, the presence of Fe^{3+} is charge-compensated by the reduction of Mn^{4+} to the larger Mn^{3+} ions, driving lattice expansion.[43] This behaviour correlates directly with the electrochemical profiles of these materials, which display an enhanced capacity contribution from the Mn^{3+}/Mn^{4+} redox plateau near 4.2 V as Fe content increases.[29] More detailed electrochemical behaviour of these Fe-substituted LMNO materials will be discussed below in Section 3.5. Fe serves as an effective modulator of TM valence states, influencing both the lattice structure and charge–compensation processes that occur during electrochemical cycling. In contrast, the comparatively smaller lattice expansion observed in Mn/Ni co-substituted materials suggests a reduced extent of Mn^{4+} reduction, consistent with smaller changes in Mn/Ni cation distribution. These findings collectively demonstrate that Fe dopants not only alter the magnitude of charge compensation but also control how local TM rearrangements

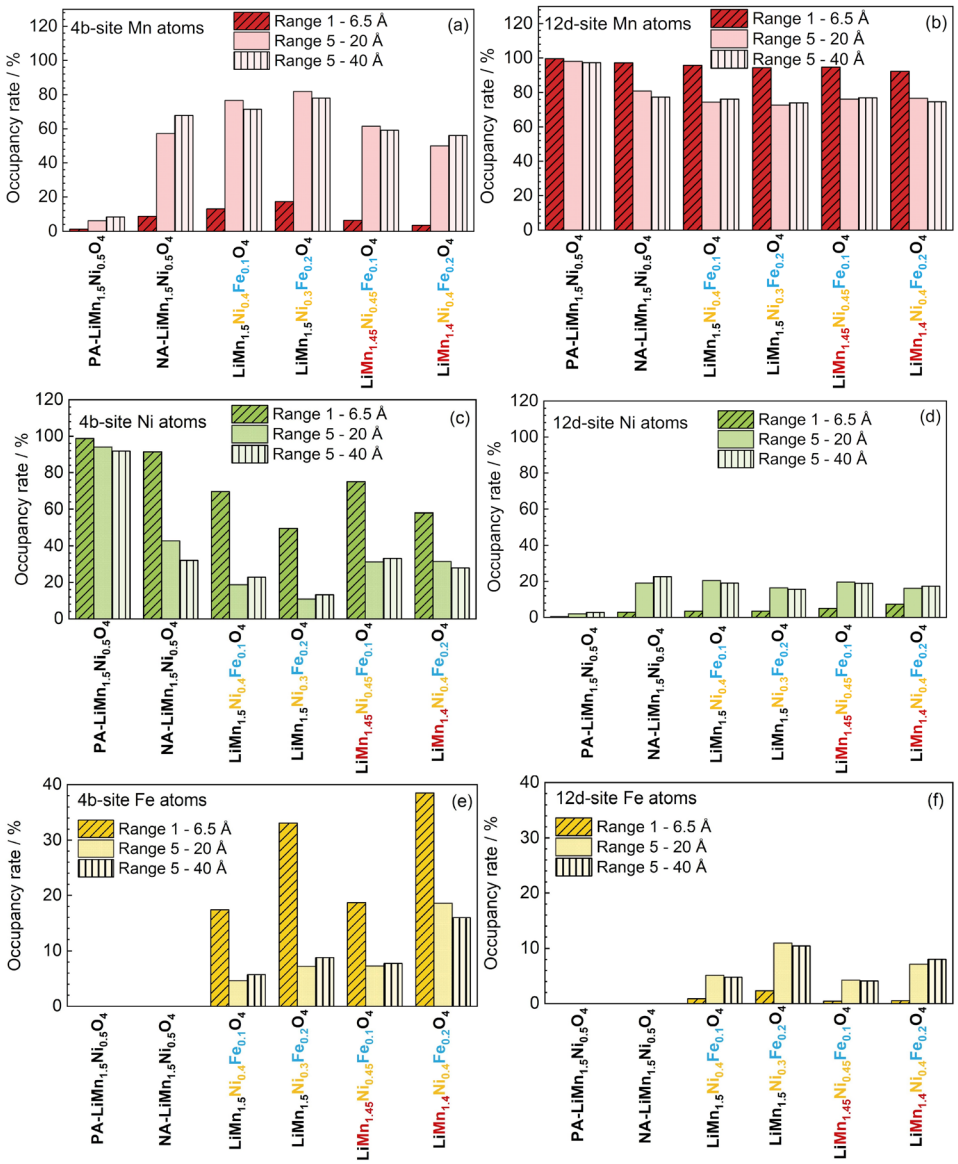

Fig. 4 Occupancy rates of Mn, Ni, and Fe atoms at the 4*b* sites (a, c, and e) and 12*d* sites (b, d, and f) for post-annealed (PA) $LiMn_{1.5}Ni_{0.5}O_4$, non-annealed (NA) $LiMn_{1.5}Ni_{0.5}O_4$, and Fe-substituted $LiMn_{1.5}Ni_{0.4}Fe_{0.1}O_4$, $LiMn_{1.5}Ni_{0.3}Fe_{0.2}O_4$, $LiMn_{1.45}Ni_{0.45}Fe_{0.1}O_4$ and $LiMn_{1.4}Ni_{0.4}Fe_{0.2}O_4$ after fitting their neutron pair distribution function data in the ranges 1–6.5 Å, 5–20 Å, and 5–40 Å, using the $P4_332$ structure model.

evolve across different length scales within the spinel framework.

3.4. Transition-metal site occupancy and substituent redistribution from local to extended length scales

Fig. 4 summarises the refined Mn, Ni, and Fe occupancies at the crystallographically distinct 4*b* and 12*d* sites in PA-LMNO, NA-LMNO, and four Fe-substituted LMNO compositions, extracted from NPDF refinements over three structural length scales (1–6.5 Å, 5–20 Å, and 5–40 Å). Over the shortest range (1–6.5 Å), both PA- and NA-LMNO retain largely ordered local environments, evidenced by high Ni occupancies at the 4*b* sites of 98.74% and 91.40%, respectively. The slightly lower Ni fraction in NA-LMNO reflects its greater degree of local Mn/Ni interchange relative to the more ordered PA-LMNO.

To rationalise the observed local-to-long-range evolution in cation occupancies, Fig. 5 illustrates how specific exchange events between Mn and Ni reshape the population of the 12*d* and 4*b* sites in the A1-type configuration. In the ideal $P4_332$ spinel (Fig. 5a), Ni exclusively occupies the 4*b* sites, while Mn fills the 12*d* sites. Localised TM disorder may occur within individual A1-type configurations *via* one-to-one cation exchange between Mn-12*d* and Ni-4*b* atoms (Fig. 5b). For instance, exchanging one Mn-12*d* with a Ni-4*b* atom per unit formula (or swapping one pair of Mn and Ni in the unit cell) reduces the Ni-4*b* site occupancy from 100% to 75% and the Mn-12*d* occupancy from 100% to ≈91.7% (Fig. 5b, denoted as one pair). A higher degree of exchange, *e.g.*, a complete replacement of all Ni-4*b* atoms by Mn atoms, with the displaced Ni atoms occupying the 12*d* sites (Fig. 5b, four pairs), further reduces the Ni-4*b* sites to 0% and decreases the Mn-12*d* sites to 66.7%. However, these simple intra-unit cell-exchange schemes (*i.e.*, swapping pairs of Mn–Ni within one unit cell) cannot account alone for the experimentally observed 1–6.5 Å TM occupancies in PA- and NA-LMNO (Tables S4 and S5) *ca.* 90% for Ni at the 4b site, which is larger than 75% under the "one pair" scheme. To rationalise this discrepancy would require inter-unit cell exchange schemes, where Mn replace the Ni(4b) in the neighbouring unit cell (Fig. 5c), producing localised TM clusters that become increasingly evident at extended length scales. Such inter-unit cell Mn–Ni exchanges align with prior observations of complex, spatially heterogeneous TM ordering in spinel LMNO.[44–46] The ordered arrangement of Mn and Ni in the other three spinel structures (A2, A3, and A4 configurations shown in Fig. 3b), after exchange *via* these mechanisms, follows the same trend in site occupancy as observed in the A1 configuration.

As the structural length scale probed by NPDF fitting increases, Mn/Ni cation exchange differences become markedly more pronounced. In PA-LMNO, Ni-4b occupation remains high at 94.01% (5–20 Å) and 91.82% (5–40 Å), indicating that the long-range structure is dominated by ordered configurations, with only minor and spatially heterogeneous Mn/Ni exchange. Conversely, NA-LMNO undergoes a substantial disordering at longer distances: Ni-4*b* occupancy drops to 42.77% at 5–20 Å and further to 32.13% at 5–40 Å, indicating extensive substitution of Ni-4*b* by Mn atoms, and a reciprocal increase of Ni atoms at the 12*d* sites. These extended-range changes confirm that NA-LMNO contains numerous Mn-rich 4*b* sites and Ni-rich 12*d* sites distributed across its structural domains, consistent with a highly disordered TM framework.

Fe-substituted LMNO materials exhibit further complexity arising from dopant-induced modifications to Mn/Ni site preference. In the 1–6.5 Å range (Fig. 4a), Mn-4*b* occupancies in the Ni-substituted materials, $LiMn_{1.5}Ni_{0.4}Fe_{0.1}O_4$ and $LiMn_{1.5}Ni_{0.3}Fe_{0.2}O_4$ (12.98% and 17.24%, respectively), exceed that of NA-LMNO (8.60%), despite identical Mn contents. This indicates that Fe incorporation promotes Mn-4*b* migration in a concentration-dependent manner and likely involves partial substitution of Mn by Fe. Over the 5–20 Å range, Mn-4*b* occupancies in these compositions increase above 75% (76.69% and 81.95%), demonstrating that certain lattice domains possess fully Mn-occupied 4*b* sites. These extended-range trends indicate the formation of Mn-rich regions whose prevalence increases with Fe content. Even at longer ranges (5–40 Å), the Mn-4*b* occupancies (71.49% and 78.20%) remain significantly high, indicating persistent spatially non-uniform TM distribution.

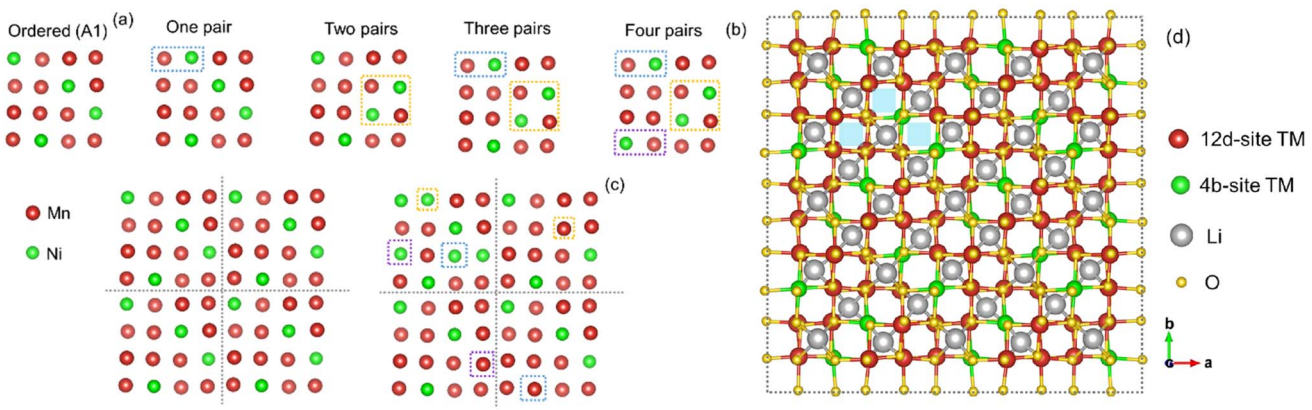

Fig. 5 Schematic representation of Mn and Ni atom distribution in the ordered spinel $LiMn_{1.5}Ni_{0.5}O_4$ (a). Ni–Mn exchange models illustrating the disordered Mn/Ni distribution within individual unit cells (intra-unit cell) (b) and between adjacent unit cells (inter-unit cell) (c); transition metal coordination environments around Li atoms (≈20 Å) (d).

The Ni distribution shows complementary behaviour. In the 1–6.5 Å range (Fig. 4c and d), Ni-4*b* occupancy differs substantially between $LiMn_{1.5}Ni_{0.4}Fe_{0.1}O_4$ (69.62%) and $LiMn_{1.5}Ni_{0.3}Fe_{0.2}O_4$ (49.66%), while the Ni-12*d* occupancies remain nearly identical ($\approx$3.5%). This implies that Fe dopants displace Ni predominantly from 4*b* sites, rather than 12*d* sites. This site specificity is confirmed by direct Fe occupancies: at short range (Fig. 4e and f), Fe shows a strong preference for 4*b* sites (17.40% in $LiMn_{1.5}Ni_{0.4}Fe_{0.1}O_4$ and 33.11% in $LiMn_{1.5}Ni_{0.3}Fe_{0.2}O_4$). However, this strong 4*b* site preference weakens as the fitting range increases. At 5–20 Å and 5–40 Å, Fe is distributed more evenly between 4*b* and 12*d* sites, indicating that Fe-induced disorder propagates over longer distances and promotes a more homogenised TM distribution at the extended scale.

The Fe site-occupancy behaviour in $LiMn_{1.45}Ni_{0.45}Fe_{0.1}O_4$ and $LiMn_{1.4}Ni_{0.4}Fe_{0.2}O_4$ follows trends consistent with the Ni-substituted compositions and is summarised in Fig. 4e, f, Tables S8 and S9. Within the short-range region (1–6.5 Å), Fe shows a strong preference for the 4*b* site, with occupancies of 18.71% and 38.50% for the two compositions. These values are significantly higher than the corresponding Fe occupancies on the 12*d* sites (0.43% and 0.50%), confirming that Fe incorporation in Mn/Ni co-substituted materials preferentially occurs at the 4*b* site. This preferential 4*b* occupation displaces Ni, driving its redistribution onto the 12*d* site, where Ni reaches 4.98% in $LiMn_{1.45}Ni_{0.45}Fe_{0.1}O_4$ and 7.34% in $LiMn_{1.4}Ni_{0.4}Fe_{0.2}O_4$ (Fig. 4d). For a fixed Fe concentration (Fig. 4e), Ni-substituted materials exhibit a lower Fe-4*b* occupancy than the Mn/Ni co-substituted samples, and this divergence increases with increasing Fe content.

At extended length scales (5–20 Å and 5–40 Å), the Mn/Ni co-substituted materials show marked reductions in Fe occupancy on the 4*b* sites, accompanied by increased Fe occupancy on 12*d* sites (Fig. 4e and f), indicating progressive redistribution as structural coherence length increases. Among all Fe-substituted compositions, $LiMn_{1.4}Ni_{0.4}Fe_{0.2}O_4$ exhibits a unique behaviour: its Fe-4*b* occupancy decreases from 18.59% (5–20 Å) to 15.97% (5–40 Å), accompanied by an occupancy decrease in Ni-4*b* and a compensating increase in Mn-4*b* (Fig. 4a and c). These changes parallel the trends observed in PA-LMNO and NA-LMNO, suggesting a common origin of the Mn/Ni disorder in these three materials that differs from the behaviour of the other Fe-substituted samples. Furthermore, these results might further indicate that co-substitution at controlled compositional limits can preserve the intrinsic TM site-occupancy preferences characteristic of LMNO.

In summary, across PA and NA-LMNO, and Fe-substituted LMNO compositions, PDF analysis reveals a clear progression in TM site occupancy from locally ordered environments to increasingly heterogeneous extended structures. While all materials show relatively ordered Mn/Ni arrangements over short length scales, long-range refinements expose substantial Mn-4*b* and Ni-12*d* redistribution in NA-LMNO and in Fe-substituted samples, consistent with extensive cation disorder at larger coherence lengths. Fe consistently prefers the 4*b* site at short range, displacing Ni and driving its migration to 12*d* positions, but this preference diminishes at longer distances as Fe, Mn, and Ni become more homogenously distributed. Notably, Mn/Ni co-substituted compositions show disorder evolution similar to NA-LMNO. Overall, these results demonstrate that cation redistribution is both range-dependent and composition-sensitive, with dopants serving as key drivers of local and extended TM disorder.

3.5. Linking local/extended cation disorder to Li-ion transport and electrochemical response

TM ordering in cathode materials directly governs the Li-ion migration landscape by modulating both the topology and the electrochemical activity of accessible redox centres.[43,47] For example, fully randomised cation arrangements maximise accessible redox centres in disordered rocksalt Li cathodes.[48] Furthermore, $LiMn_{1.4}Ni_{0.4}Fe_{0.2}O_4$ demonstrates significantly enhanced rate performance and cycling stability at 20C relative to LMNO calcined at 1000 °C.[47] Similarly, Fe substitution by Mn and Ni in Li-rich $Li_{1.2}Mn_{0.6}Ni_{0.2}O_2$ has been shown to improve its Li-ion diffusion and mitigates Ni migration into Li sites.[5]

As established from our NPDF refinements, LMNO and Fe-substituted derivatives exhibit distinct degrees of cation disorder that evolve from locally ordered (1–6.5 Å) to increasingly heterogeneous extended structures (5–40 Å). These structural variations translate directly into differences in Li-diffusion environments, redox behaviour, and rate capability.

In the ideal $P4_332$ spinel arrangement, each Li atom is coordinated by three 12*d*-site and one 4*b*-site TM neighbours, producing various diffusion environments (highlighted in blue in Fig. 5d). However, the introduction of Mn/Ni exchange, and especially Fe substitution, produces a distribution of local Li-migration geometries, including (i) three-12*d*/one-4*b*, (ii) two-12*d*/two-4*b*, and (iii) four-12*d* TM configurations. Our PDF results show that such environments proliferate in NA-LMNO and in all Fe-substituted compositions, particularly over extended length scales where Fe, Mn, and Ni become increasingly redistributed across both TM sites. These mixed cation environments modify local TM–O bond lengths, the electrostatic landscape experienced by Li, and the energy barriers for Li hopping. As a result, compositional and spatial fluctuations in TM occupancy directly shape lithium transport and, consequently, the electrochemical signature of these materials.[43,47]

These structural effects are mirrored in the galvanostatic cycling shown in Fig. 6. Ni-substituted samples ($LiMn_{1.5}Ni_{0.4}Fe_{0.1}O_4$ and $LiMn_{1.5}Ni_{0.3}Fe_{0.2}O_4$) exhibit enhanced Mn^{3+}/Mn^{4+} activity near 4.1 V relative to NA-LMNO, consistent with Fe^{3+} substitution for Ni^{2+} ions, and the charge-compensating generation of Mn^{3+} ions.[29] The corresponding expansion of the *a* parameter (see Section 3.3) and different redox peak intensities shown in the d*Q*/d*V* plots (Fig. 6b) reflect the modified local coordination environments observed by NPDF in these compositions. Likewise, the suppressed and shifted Ni^{2+}/Ni^{4+} redox activity between 4.6–4.8 V is consistent with our observation that Fe preferentially occupies 4*b* sites at short range, displacing Ni toward 12*d* sites and disrupting its ordered electronic environment.

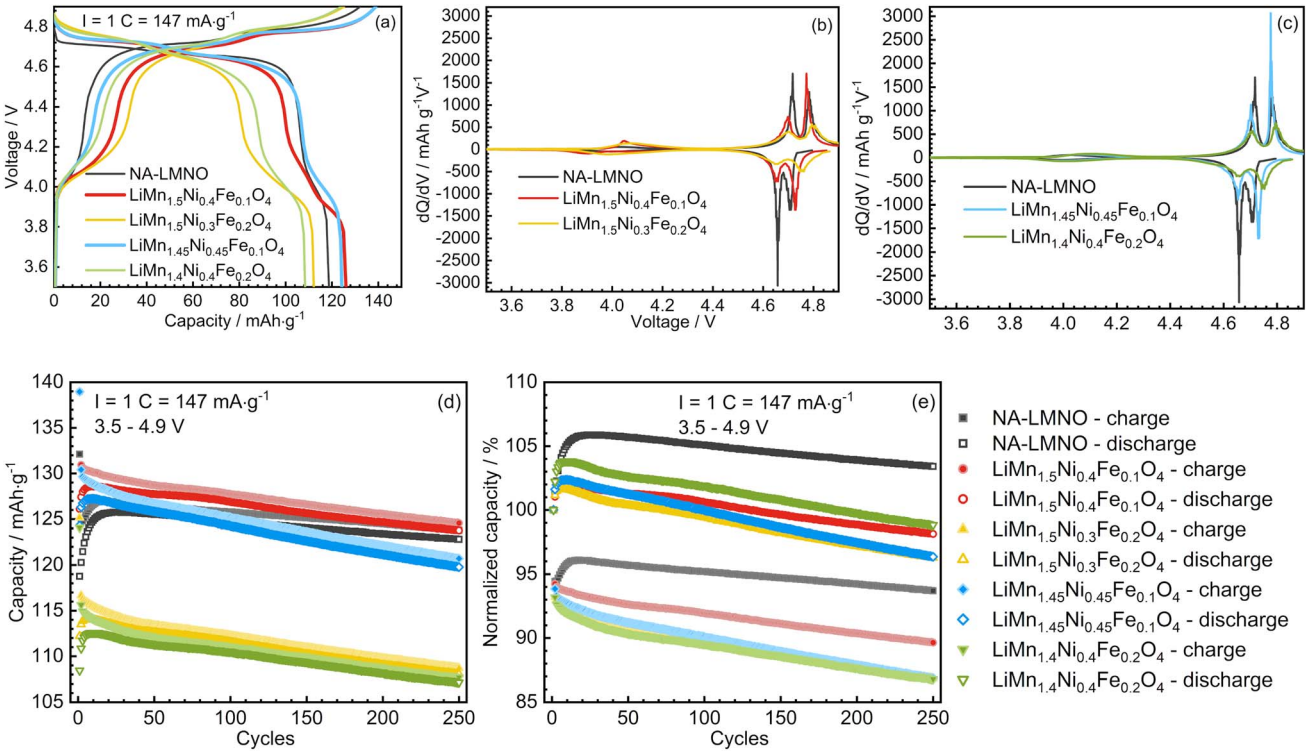

Fig. 6 Initial charge and discharge load profiles (a), initial dQ/dV *vs.* V plots (b) and (c), specific capacity *vs.* cycle number (d), and normalised capacity *vs.* cycle number (e) of non-annealed (NA) $LiMn_{1.5}Ni_{0.5}O_4$, $LiMn_{1.5}Ni_{0.4}Fe_{0.1}O_4$, $LiMn_{1.5}Ni_{0.3}Fe_{0.2}O_4$, $LiMn_{1.45}Ni_{0.45}Fe_{0.1}O_4$ and $LiMn_{1.4}Ni_{0.4}Fe_{0.2}O_4$ at a current density of 147 mA g^{-1} in the voltage range of 3.5–4.9 V.

Mn/Ni co-substituted compositions ($LiMn_{1.45}Ni_{0.45}Fe_{0.1}O_4$ and $LiMn_{1.4}Ni_{0.4}Fe_{0.2}O_4$) reveal a distinct behaviour: although Fe should not theoretically change the nominal TM valence states compared to NA-LMNO, their non-uniform Fe distributions, evidenced by NPDF-derived long-range cation gradients, produce spatially varying Mn and Ni redox environments. These samples exhibit modified plateau intensities near both the Mn and Ni redox regions (Fig. 6a and c), signalling heterogeneous local electronic structures created by the Fe-regulated cation arrangements.

The influence of Fe concentration on capacity is directly correlated with its impact on TM disorder. Initial discharge capacities of $LiMn_{1.5}Ni_{0.4}Fe_{0.1}O_4$ and $LiMn_{1.45}Ni_{0.45}Fe_{0.1}O_4$ are 126.1 and 124.3 mA h g^{-1}, which are higher than that of NA-LMNO (118.8 mA h g^{-1}) (Fig. 6d and e). This indicates that moderate Fe substitution ($x = 0.05$) yields higher initial capacities and improved cycling stability relative to NA-LMNO. This improvement aligns with NPDF evidence that shows that this sample introduces controlled disorder, expanding the diversity of Li-migration environments without fully disrupting long-range structural coherence.

In contrast, higher Fe content ($x = 0.1$) leads to capacity degradation in both Ni-substituted and Mn/Ni co-substituted materials, being the capacity fade trend almost identical for both samples. The capacity decay is attributed to altered charge compensation mechanisms in the Fe-doped samples. The introduction of Fe, which undergoes redox processes above 4.9 V within the spinel structure, enhances the contribution of the Mn^{3+}/Mn^{4+} redox couple to capacity. This increased manganese activity promotes the disproportionation of Mn^{3+} into Mn^{2+} and Mn^{4+} atoms, while dissolution of Mn^{2+} into the electrolyte is a cause of the cycling performance deterioration.[32] At this level, NPDF refinements show substantial redistribution of Fe onto 12*d* sites at extended ranges, producing broad structural heterogeneity that hinders Ni redox activity and introduces kinetic limitations during Li extraction. Notably, Fe-substituted samples no longer exhibit activation, characteristic of charge capacity during cycling of NA-LMNO (Fig. 6e). This suggests that Fe-induced cation redistribution may stabilise Li diffusion pathways and suppress the local structural transformations associated with activation.

Overall, the combined NPDF and electrochemical analyses demonstrate that Fe substitution modifies performance not simply by altering composition, but by reshaping the spatial distribution of Mn, Ni, and Fe across different structural length scales. The resulting evolution of Li-migration environments provides a structural framework for understanding the tuneable redox behaviour and rate capability of Fe-modified LMNO.

4. Conclusions

This work establishes a direct, multiscale link between TM site occupancy, dopant-driven cation redistribution, and electrochemical performance in high-voltage spinel LMNO-based cathodes. Through detailed neutron PDF analysis, we show that both PA-LMNO and NA-LMNO retain a predominantly

ordered Mn/Ni arrangement at short range (1–6.5 Å), driven by the intrinsic preference of Mn and Ni for the 12*d* and 4*b* sites, respectively. At longer structural length scales (5–40 Å), however, significant divergence emerges: NA-LMNO develops extensive Mn–Ni exchange within and between lattices, generating a heterogeneous mosaic of locally ordered and disordered domains, absent in the post-annealed analogue.

Fe substitution introduces an additional layer of complexity. All Fe-containing compositions display site-selective dopant behaviour, with Fe^{3+} occupying Ni-4*b* sites at short range, yet increasingly populating Mn-12*d* sites as structural disorder propagates across extended distances. This progressive redistribution perturbs the local TM coordination landscape, amplifies Mn/Ni/Fe heterogeneity across domains, and produces a wider set of Li-migration environments than in pristine LMNO. Notably, the balance between short-range selectivity and long-range redistribution differs between Ni-substituted and Mn/Ni co-substituted compositions, underscoring the sensitivity of Fe-site preference to the surrounding cation chemistry.

These structural findings correlate strongly with the observed electrochemical behaviour. Moderate Fe substitution ($x = 0.05$) in LMNO enhances Mn^{3+}/Mn^{4+} redox activity near 4.2 V, modifies Ni^{2+}/Ni^{4+} contributions between 4.6–4.8 V, and suppresses the activation process characteristic of undoped NA-LMNO, which is also consistent with changes in lattice size and regulation of local Li–diffusion pathways evidenced by NPDF investigation. Higher Fe levels ($x = 0.1$), where NPDF refinements show more pervasive long-range cation disorder, lead to diminished capacity and accelerated fading, illustrating that the extent of disorder, and not merely its presence, is critical. Optimal performance, therefore, arises from controlled cation heterogeneity, where Fe subtly reshapes the TM lattice without generating excessive structural incoherence.

Overall, this study provides a unified structural–electrochemical framework for understanding how dopant distribution across local and extended length scales governs Li transport and redox processes in high-voltage spinels. By combining tailored substitution chemistry with quantitative short- and extended-range NPDF analysis, we demonstrate a general strategy for rationally tuning cation order, migration pathways, and functional performance. This approach may be broadly applicable to complex transition-metal oxide cathodes for Li-ion and next-generation energy storage systems, offering a pathway toward the predictive design of cathode materials with enhanced stability and rate capability.

Conflicts of interest

There are no conflicts of interest to declare.

Data availability

The data supporting this article have been included as part of the supplementary information (SI). Supplementary information is available. See DOI: https://doi.org/10.1039/d5ta10430k.

Acknowledgements

This research was supported by the Faraday Institution under grant FIRG065 (FutureCat project). N. T.-R. gratefully acknowledges the Leverhulme Doctoral Scholarships Program in 'Material Social Futures' (DS-2017-036) for providing a PhD studentship to B. E. M. The authors gratefully acknowledge the assistance of Dr Gabriel-Perez and Dr Helen Playford on the GEM beamline at the ISIS Neutron and Muon Source (Proposal 2000201).

References

1 C. Vaalma, *et al.*, A cost and resource analysis of sodium-ion batteries, *Nat. Rev. Mater.*, 2018, **3**, 18013.
2 P. Oh, *et al.*, Recent advances and prospects of atomic substitution on layered positive materials for lithium-ion battery, *Adv. Energy Mater.*, 2021, **11**, 2003197.
3 H. Xu, *et al.*, Mainstream optimization strategies for cathode materials of sodium-ion batteries, *Small Struct.*, 2022, **3**, 2100217.
4 Y. Xiao, *et al.*, Layered oxide cathodes promoted by structure modulation technology for sodium-ion batteries, *Adv. Funct. Mater.*, 2020, **30**, 2001334.
5 F. Wu, *et al.*, Elucidating the effect of iron doping on the electrochemical performance of cobalt-free lithium-rich layered cathode materials, *Adv. Energy Mater.*, 2019, **9**, 1902445.
6 J. Billaud, *et al.*, Li/Fe substitution in Li-rich Ni, Co, Mn oxides for enhanced electrochemical performance as cathode materials, *J. Mater. Chem. A*, 2019, **7**, 15215–15224.
7 Q. Wang, *et al.*, Morphology control and Na^+ doping toward high-performance Li-rich layered cathode materials for lithium-ion batteries, *ACS Sustain. Chem. Eng.*, 2020, **9**, 197–206.
8 N. Bucher, *et al.*, P2-$Na_xCo_yMn_{1-y}O_2$ (y= 0, 0.1) as cathode materials in sodium-ion batteries effects of doping and morphology to enhance cycling stability, *Chem. Mater.*, 2016, **28**, 2041–2051.
9 K. Tang, *et al.*, High-performance P2-Type Fe/Mn-based oxide cathode materials for sodium-ion batteries, *Electrochim. Acta*, 2019, **312**, 45–53.
10 M. H. Han, *et al.*, A comprehensive review of sodium layered oxides: Powerful cathodes for Na-ion batteries, *Energy Environ. Sci.*, 2015, **8**, 81–102.
11 M. S. Whittingham, *et al.*, Lithium batteries and cathode materials, *Chem. Rev.*, 2004, **104**, 4271–4302.
12 A. Manthiram, *et al.*, A reflection on lithium-ion battery cathode chemistry, *Nat. Commun.*, 2020, **11**, 1550.
13 Y. Fan, *et al.*, Fundamental understanding and practical challenges of lithium-rich oxide cathode materials: Layered and disordered-rocksalt structure, *Energy Storage Mater.*, 2021, **40**, 51–71.
14 X. Yu, *et al.*, Advances and prospects of high-voltage spinel cathodes for lithium-based batteries, *Small Methods*, 2021, **5**, 2001196.

15 P. Wang, *et al.*, Layered oxide cathodes for sodium-ion batteries: phase transition, air stability, and performance, *Adv. Energy Mater.*, 2018, **8**, 1701912.
16 J. Zheng, *et al.*, Role of superexchange interaction on tuning of Ni/Li disordering in layered $Li(Ni_xMn_yCo_z)O2$, *J. Phys. Chem. Lett.*, 2017, **8**, 5537–5542.
17 Z. Li, *et al.*, Improving the performance of layered oxide cathode materials with football-like hierarchical structure for Na-ion batteries by incorporating Mg^{2+} into vacancies in Na-ion layers, *ChemSusChem*, 2018, **11**, 1223–1231.
18 Z. Cai, *et al.*, In situ formed partially disordered phases as earth-abundant Mn-rich cathode materials, *Nat. Energy*, 2023, **9**, 27–36.
19 H. Ji, *et al.*, Ultrahigh power and energy density in partially ordered lithium-ion cathode materials, *Nat. Energy*, 2020, **5**, 213–221.
20 C. S. Yoon, *et al.*, Cation ordering of Zr-doped $LiNiO_2$ cathode for lithium-ion batteries, *Chem. Mater.*, 2018, **30**, 1808–1814.
21 R. Shunmugasundaram, *et al.*, A study of stacking faults and superlattice ordering in some Li-rich layered transition metal oxide positive electrode materials, *J. Electrochem. Soc.*, 2016, **163**, A1394.
22 Z. Lu, *et al.*, Superlattice ordering of Mn, Ni, and Co in layered alkali transition metal oxides with P2, P3, and O3 structures, *Chem. Mater.*, 2000, **12**, 3583–3590.
23 J. Paulsen, *et al.*, Layered T2-, O6-, O2-, and P2-Type A2/3 $[M'^{2+}_{1/3}M^{4+}_{2/3}]O_2$ Bronzes, A= Li, Na; M'= Ni, Mg; M= Mn, Ti, *Chem. Mater.*, 2000, **12**, 2257–2267.
24 J. Cheng, *et al.*, Enhancing surface oxygen retention through theory-guided doping selection in $Li_{1-x}NiO_2$ for next-generation lithium-ion batteries, *J. Mater. Chem. A*, 2020, **8**, 23293–23303.
25 J. Bréger, *et al.*, Short-and long-range order in the positive electrode material, $Li(NiMn)_{0.5}O_2$: A joint X-ray and neutron diffraction, pair distribution function analysis and NMR study, *J. Am. Chem. Soc.*, 2005, **127**, 7529–7537.
26 D. Zeng, *et al.*, Cation ordering in $Li[Ni_xMn_xCo_{(1-2x)}]O_2$-layered cathode materials: A nuclear magnetic resonance (NMR), pair distribution function, X-ray absorption spectroscopy, and electrochemical Study, *Chem. Mater.*, 2007, **19**, 6277–6289.
27 Z. Moorhead-Rosenberg, *et al.*, Electronic and electrochemical properties of $Li_{1-x}Mn_{1.5}Ni_{0.5}O_4$ spinel cathodes as a function of lithium content and cation ordering, *Chem. Mater.*, 2015, **27**, 6934–6945.
28 J. Liu, *et al.*, Nanoscale Ni/Mn ordering in the high voltage spinel cathode $LiNi_{0.5}Mn_{1.5}O_4$, *Chem. Mater.*, 2016, **28**, 6817–6821.
29 B. E. Murdock, *et al.*, Li-Site Defects induce formation of Li-rich impurity phases: Implications for charge distribution and performance of $LiNi_{0.5-x}M_xMn_{1.5}O_4$ cathodes (M= Fe and Mg; x= 0.05–0.2), *Adv. Mater.*, 2024, **36**, 2400343.
30 I. Ahmed, *et al.*, Mechanism of iron integration into $LiMn_{1.5}Ni_{0.5}O_4$ for the electrocatalytic oxygen evolution reaction, *Energy Fuel.*, 2022, **36**, 12160–12169.
31 Y. Gao, *et al.*, Fe doping in $LiMn_{1.5}Ni_{0.5}O_4$ by atomic layer deposition followed by annealing: depths and occupation sites, *J. Phys. Chem. C*, 2021, **125**, 7560–7567.
32 A. Windmüller, et al., Structural insights into Ni-stabilized Fe-rich high-voltage spinels: $LiNi_xFe_{0.5-x}Mn_{1.5}O_4$, *Small Struct.*, 2025, 2400691.
33 E. Rossen, *et al.*, Synthesis and electrochemistry of spinel LT-$LiCoO_2$, *Solid State Ionics*, 1993, **62**, 53–60.
34 Z. Wu, et al., Does "zero-strain" lithiated spinel serve as a strain retardant and an irreversible phase transition regulator for layered oxide cathodes?, *Chem. Sci.*, 2024, **15**, 16752–16759.
35 B. Shi, et al., LT-$LiMn_{0.5}Ni_{0.5}O_2$: A unique co-free cathode for high energy Li-ion cells, *Chem. Commun.*, 2021, **57**, 11009–11012.
36 Z. Cai, et al., In situ formed partially disordered phases as earth-abundant Mn-rich cathode materials, *Nat. Energy*, 2024, **9**, 27–36.
37 W. G. Williams, *et al.*, GEM—general materials diffractometer at ISIS, *Phys. B*, 1997, **241**, 234–236.
38 A. K. Soper, *GudrunN and GudrunX: Programs for Correcting Raw Neutron and X-Ray Diffraction Data to Differential Scattering Cross Section*, Science & Technology Facilities Council, Swindon, UK, 2011.
39 C. Farrow, *et al.*, PDFfit2 and PDFgui: computer programs for studying nanostructure in crystals, *J. Phys.: Condens. Matter*, 2007, **19**, 335219.
40 V. F. Sears, Neutron scattering lengths and cross sections, *Neutron News*, 1992, **3**, 26–37.
41 J. Rana, *et al.*, Local structural changes in $LiMn_{1.5}Ni_{0.5}O_4$ spinel cathode material for lithium-ion batteries, *J. Power Sources*, 2014, **255**, 439–449.
42 P. B. Samarasingha, *et al.*, In situ synchrotron study of ordered and disordered $LiMn_{1.5}Ni_{0.5}O_4$ as lithium ion battery positive electrode, *Acta Mater.*, 2016, **116**, 290–297.
43 H. Duncan, *et al.*, Relationships between Mn^{3+} content, structural ordering, phase transformation, and kinetic properties in $LiNi_xMn_{2-x}O_4$ cathode materials, *Chem. Mater.*, 2014, **26**, 5374–5382.
44 G. Lim, *et al.*, Regulating dynamic electrochemical interface of $LiNi_{0.5}Mn_{1.5}O_4$ spinel cathode for realizing simultaneous Mn and Ni redox in rechargeable lithium batteries, *Adv. Energy Mater.*, 2022, **12**, 2202049.
45 M. Lin, *et al.*, Insight into the atomic structure of high-voltage spinel $LiNi_{0.5}Mn_{1.5}O_4$ cathode material in the first cycle, *Chem. Mater.*, 2015, **27**, 292–303.
46 S. L. Spence, *et al.*, Mapping lattice distortions in $LiNi_{0.5}Mn_{1.5}O_4$ cathode materials, *ACS Energy Lett.*, 2022, **7**, 690–695.
47 N. Kiziltas-Yavuz, *et al.*, Enhancement of electrochemical performance by simultaneous substitution of Ni and Mn with Fe in Ni-Mn spinel cathodes for Li-ion batteries, *J. Power Sources*, 2016, **327**, 507–518.
48 Y. Wang, *et al.*, Unraveling the nature and role of layered cation ordering in cation-disordered rock-salt cathodes, *J. Am. Chem. Soc.*, 2022, **144**, 19838–19848.